inorganics

MDPI

Article

The Conversion Polymorphism of Perovskite Phases in the $BiCrO_3$–$BiFeO_3$ System

Alexei A. Belik

Research Center for Materials Nanoarchitectonics (MANA), National Institute for Materials Science (NIMS), Namiki 1-1, Tsukuba 305-0044, Ibaraki, Japan; alexei.belik@nims.go.jp

Abstract: Perovskite-type materials containing Bi^{3+} cations at A sites are interesting from the viewpoints of applications and fundamental science as the lone pair of Bi^{3+} cations often stabilizes polar, ferroelectric structures. This can be illustrated by a lot of discoveries of different new functionalities in bulk and thin films of $BiFeO_3$ and its derivatives. In this work, we investigated solid solutions of $BiCr_{1-x}Fe_xO_3$ with $0.1 \leq x \leq 0.4$ prepared by a high-pressure (HP) method and post-synthesis annealing at ambient pressure (AP). HP-$BiCr_{1-x}Fe_xO_3$ modifications with $0.1 \leq x \leq 0.3$ were mixtures of two phases with space groups $C2/c$ and *Pbam*, and the amount of the $C2/c$ phase decreased with increasing x. The amount of the $C2/c$ phase was also significantly decreased in AP-$BiCr_{1-x}Fe_xO_3$ modifications, and the $C2/c$ phase almost disappeared in AP-$BiCr_{1-x}Fe_xO_3$ with $0.2 \leq x \leq 0.3$. Fundamental, strong reflections of HP-$BiCr_{1-x}Fe_xO_3$ and AP-$BiCr_{1-x}Fe_xO_3$ were almost unchanged; on the other hand, weak superstructure reflections were different and showed clear signs of strong anisotropic broadening and incommensurate positions. These structural features prevented us from determining their room-temperature structures. On the other hand, HP-$BiCr_{1-x}Fe_xO_3$ and AP-$BiCr_{1-x}Fe_xO_3$ showed high-temperature structural phase transitions to the $GdFeO_3$-type *Pnma* modification at T_{srt} = 450 K (x = 0.1), T_{srt} = 480 K (x = 0.2), T_{srt} = 510 K (x = 0.3), and T_{srt} = 546 K (x = 0.4). Crystal structures of the $GdFeO_3$-type *Pnma* modifications of all the samples were investigated by synchrotron powder X-ray diffraction. Magnetic properties of HP-$BiCr_{1-x}Fe_xO_3$ and AP-$BiCr_{1-x}Fe_xO_3$ were quite close to each other (HP vs. AP), and the x = 0.2 samples demonstrated negative magnetization phenomena without signs of the exchange bias effect.

Keywords: multiferroics; doped $BiFeO_3$; $BiCrO_3$; high-pressure synthesis; irreversible transformations; conversion polymorphism; incommensurate structures

Academic Editors: Jianhua Han, Yuyu Su and Xuanling Liu

Received: 25 February 2025
Revised: 12 March 2025
Accepted: 14 March 2025
Published: 18 March 2025

Citation: Belik, A.A. The Conversion Polymorphism of Perovskite Phases in the $BiCrO_3$–$BiFeO_3$ System. *Inorganics* **2025**, *13*, 91. https://doi.org/10.3390/inorganics13030091

1. Introduction

Bi^{3+} cations have a lone electron pair similar to Pb^{2+} cations and, therefore, are often considered as a replacement of toxic lead in ferroelectric and piezoelectric materials. $BiFeO_3$ perovskite has been known since the late 1950s [1–4]. However, it has received tremendous interest in the 2000s [5,6] after the discovery that thin films of $BiFeO_3$ can have good ferroelectric properties and are effective and model multiferroic materials [7–9]. Since then, thousands of publications have been devoted to $BiFeO_3$ perovskite and its derivatives [6]. A lot of fundamental science and practical discoveries have recently been made using $BiFeO_3$ perovskite [10–14], for example, related to manipulations of charge domain walls, chiral spin transport, and spin cycloids, the formation of skyrmion lattices, and so on.

$BiFeO_3$ crystallizes in space group $R3c$ below its ferroelectric transition temperature T_{FE} = 1100 K, and it shows a number of high-temperature structural transitions [6]. Its first transition at T_{FE} is to a $GdFeO_3$-type *Pnma* phase [15], not to a centrosymmetric pair

(space group *R*-3*c*) of space group *R*3*c* as one would expect. The ferroelectricity of $BiFeO_3$ originates from the activity of the lone electron pair of Bi^{3+} cations [6]. The pure antiferromagnetic (AFM) transition occurs at the Néel temperature T_N = 643 K and originates from superexchange interactions between magnetic Fe^{3+} cations [6]. The absence of any net ferromagnetic (FM) moments in $BiFeO_3$ originates from long-period incommensurate spin ordering, which averages the total net moment to zero [6]. $BiFeO_3$ perovskite is the only compound among other simple $BiMO_3$ perovskites that can be prepared in bulk form under ambient pressure (AP) conditions.

$BiCrO_3$ perovskite has been known since the middle of the 1960s [16–18], but it received renewed interest in the 2000s [19–31] as a counterpart to $BiFeO_3$. It crystallizes in space group *C*2/*c* at room temperature (RT) and shows a structural phase transition to a $GdFeO_3$-type *Pnma* modification above T_{str} = 420 K [23,24]. $BiCrO_3$ demonstrates an AFM transition at T_N = 112 K to a G-type AFM structure with small spin canting (and, therefore, with the appearance of weak FM properties) [23–26,30,31], and there is a spin-reorientation transition near 72–75 K with an increased weak FM moment. $BiCrO_3$ perovskite can only be stabilized in bulk form under high-pressure (HP) synthesis conditions [32].

Other simple $BiMO_3$ perovskites have been studied less because they need an HP high-temperature method for their preparation in bulk form [32]. It is interesting that there are many structural variations in simple $BiMO_3$ perovskites [27,32]: samples with M = Sc, Cr, and Mn crystallize in space group *C*2/*c*; M = Al and Fe samples—in polar space group *R*3*c*; the M = Co sample—in polar space group *P*4*mm*; the M = Ni sample—in space group *P*-1; the M = Ga sample—in a pyroxene-type (non-perovskite) *Pcca* structure; and the M = Rh sample—in space group *Pnma* [32]. Therefore, different $BiM1_{1-x}M2_xO_3$ solid solutions can show complex structural variations and transformations as a function of composition *x* and temperature. Such solid solutions have received a tremendous amount of interest in the literature [33–51]. For example, the appearance of polar *R*3*c* phases was observed in the solid solution system between centrosymmetric $BiCrO_3$ and $BiGaO_3$ [47,50]. In the solid solutions between $BiFeO_3$ and $BiCrO_3$, one composition has been investigated a lot, namely Bi_2FeCrO_6, after the first-principle predictions [52] that this composition (with ordered arrangements of Fe^{3+} and Cr^{3+} cations) should show large ferroelectric polarization and large magnetization [53–58]. In particular, thin films of Bi_2FeCrO_6 have attracted a lot of attention from the application point of view as photovoltaic materials [57,58]. The number of investigations focusing on properties of bulk $BiCr_{1-x}Fe_xO_3$ solid solutions is very limited because such solid solutions need an HP method for their preparation [59–64], and the majority of such studies are focused on studies of Fe-rich samples [60–62].

Therefore, in this work we investigated samples from the Cr-rich side of bulk $BiCr_{1-x}Fe_xO_3$ solid solutions with $0.1 \leq x \leq 0.4$. We found structural phase transitions to the *Pnma* modification with systematic changes in the phase transition temperature. We found that the as-synthesized samples do not transform back into their initial state after cooling from high temperatures, therefore realizing the conversion polymorphism phenomenon [41]. Weak incommensurate structural modulations were found in $BiCr_{1-x}Fe_xO_3$ solid solutions with $0.1 \leq x \leq 0.4$. Detailed magnetic properties are reported.

2. Results and Discussion

All $BiCr_{1-x}Fe_xO_3$ samples contained small amounts of $Bi_2O_2CO_3$ impurity. The *x* = 0.1 and 0.2 samples additionally contained very small amounts of Cr_2O_3 impurity; the amount of Cr_2O_3 impurity was at the background level in the *x* = 0.3 and 0.4 samples. HP-$BiCr_{1-x}Fe_xO_3$ samples with *x* = 0.1, 0.2, and 0.3 consisted of two perovskite-type modifications: one modification had the *C*2/*c* symmetry as found in undoped $BiCrO_3$ [24], and the second modification had the $PbZrO_3$-type structure (space group *Pbam* (No. 55)

and a $\sqrt{2}a_p \times 2\sqrt{2}a_p \times 2a_p$ superstructure, where a_p (≈3.95 Å) is the parameter of the cubic perovskite subcell [62,65,66]). The amount of the $BiCrO_3$-type $C2/c$ modification rapidly decreased with increasing x from about 75% (x = 0.1) to about 50% (x = 0.2) and about 5% (x = 0.3) in the HP samples (Figures 1 and 2). The amount of the $BiCrO_3$-type $C2/c$ modification also rapidly decreased with increasing x from about 40% (x = 0.1) to trace amounts (x = 0.2) to undetectable amounts (x = 0.3) in the AP samples (Figures 1 and 2). Both HP- and AP-$BiCr_{0.6}Fe_{0.4}O_3$ contained only a perovskite phase with the $PbZrO_3$-type structure (Figure 2b).

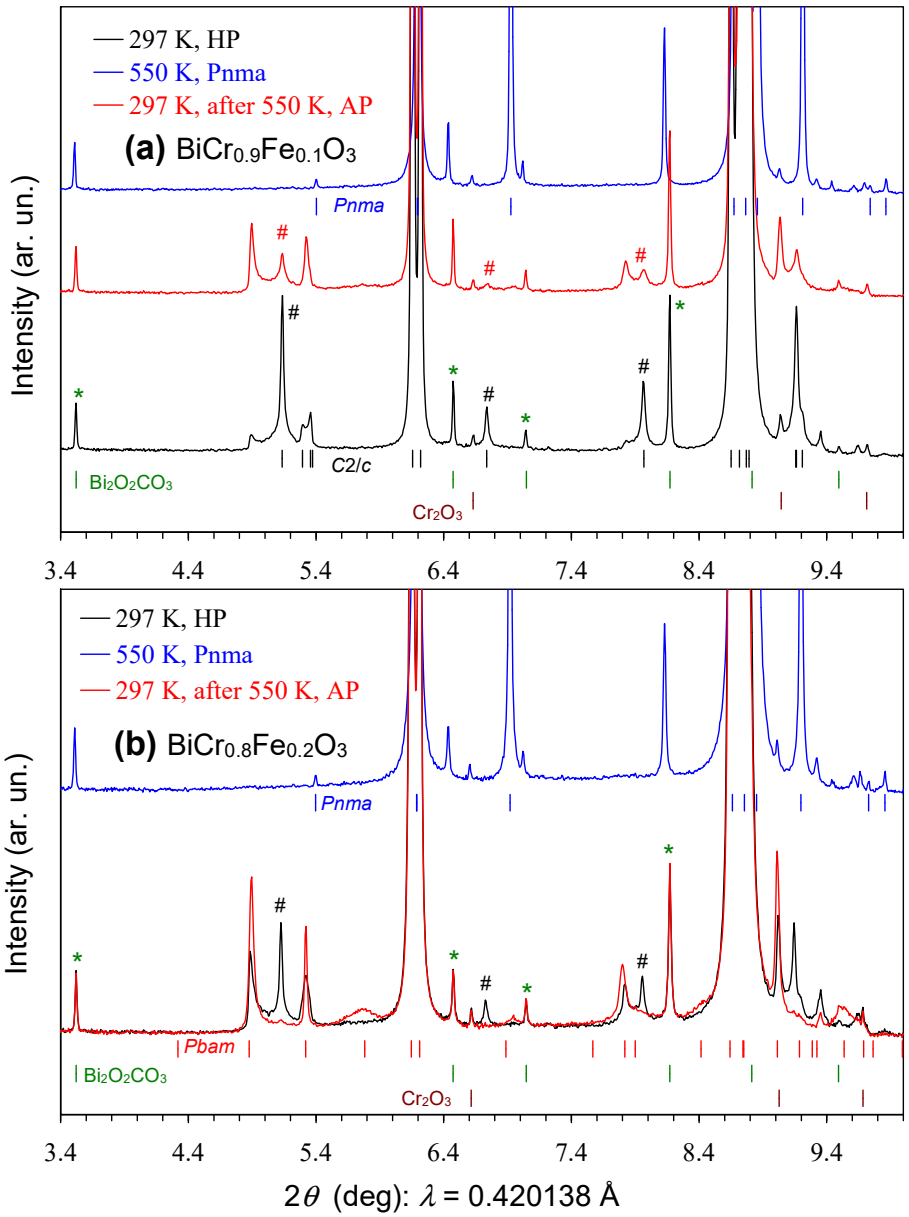

Figure 1. Magnified fragments of experimental synchrotron powder X-ray diffraction patterns of (**a**) $BiCr_{0.9}Fe_{0.1}O_3$ and (**b**) $BiCr_{0.8}Fe_{0.2}O_3$. Patterns for the as-synthesized HP modifications at T = 297 K are shown by black lines, for the *Pnma* modifications at T = 550 K—by blue lines, and the AP modifications at T = 297 K—by red lines. The tick marks show possible Bragg reflection positions for the main perovskite phases ($C2/c$, *Pnma*, and *Pbam*) and $Bi_2O_2CO_3$ and Cr_2O_3 impurities. The characteristic reflections of the $C2/c$ modification are additionally marked by black/red octothorps. The characteristic reflections of the $Bi_2O_2CO_3$ impurity are additionally marked by green stars.

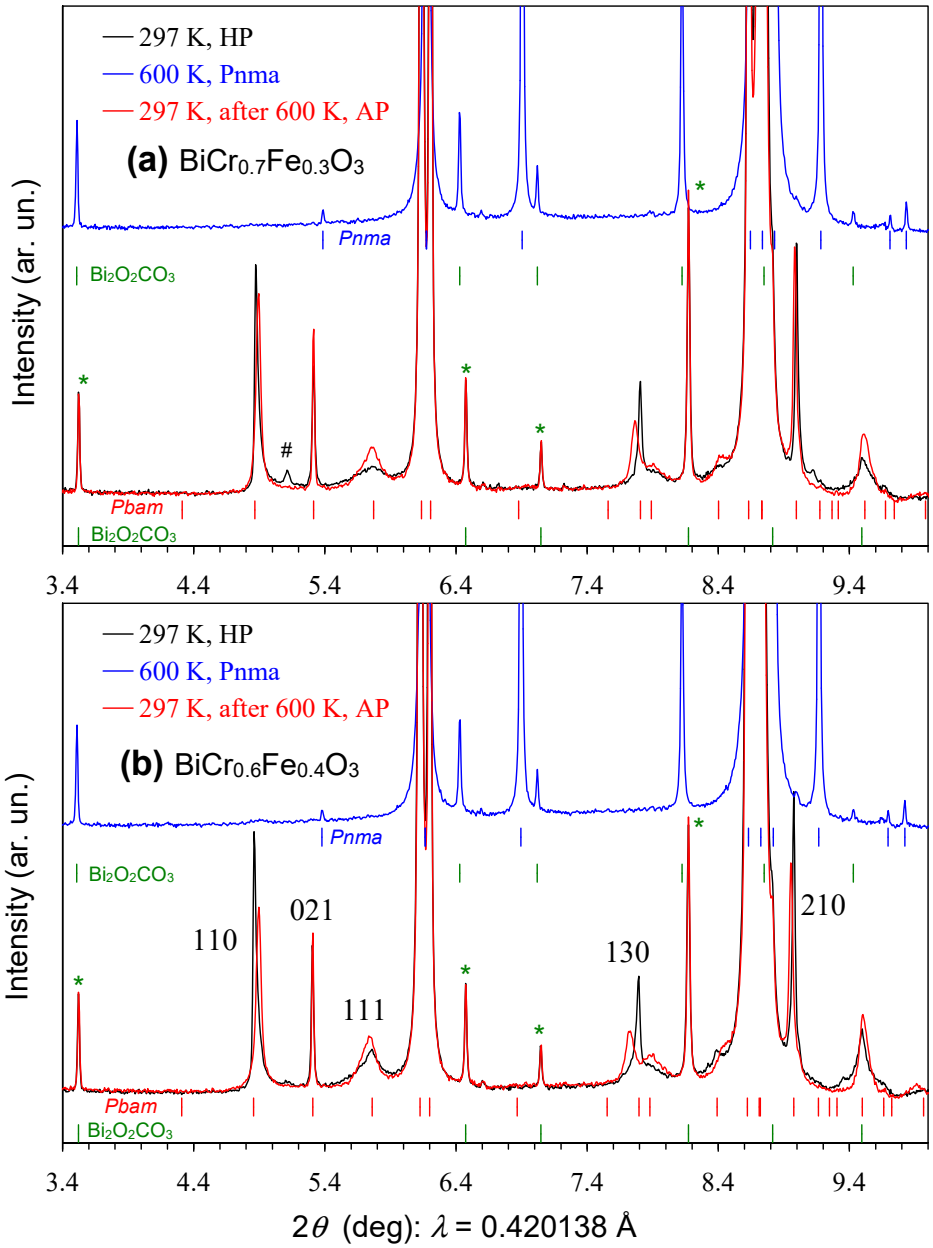

Figure 2. Magnified fragments of experimental synchrotron powder X-ray diffraction patterns of (**a**) $BiCr_{0.7}Fe_{0.3}O_3$ and (**b**) $BiCr_{0.6}Fe_{0.4}O_3$. Patterns for the as-synthesized HP modifications at T = 297 K are shown by black lines, for the *Pnma* modifications at T = 600 K—by blue lines, and the AP modifications at T = 297 K—by red lines. The tick marks show possible Bragg reflection positions for the main perovskite phases (*Pnma* and *Pbam*) and $Bi_2O_2CO_3$ impurity. The characteristic reflections of the $C2/c$ modification are marked by black octothorps. The characteristic reflections of the $Bi_2O_2CO_3$ impurity are additionally marked by green stars. (*hkl*) indices of some superstructure reflections of the *Pbam*-related modification are given.

Figure 3 shows the results of the DSC measurements. All samples demonstrated a reversible phase transition with sharp peaks on the DSC heating curves at T_{str} = 450 K (x = 0.1), 480 K (x = 0.2), 510 K (x = 0.3), and 546 K (x = 0.4), where T_{str} stands for the structural phase transition temperature. The first heating curve was slightly different from the second and third heating curves; all cooling curves were almost identical. The small difference between the heating curves can be explained by the fact the HP modification transforms to the AP modification after the first DSC run. The synchrotron XRD data (Figures 1 and 2; blue curves) clearly showed that the DSC anomalies corre-

spond to a structural phase transition to the *Pnma* modification. With T_{str} = 420 K for undoped $BiCrO_3$ [23,24], T_{str} almost linearly increases with increasing x in the $BiCr_{1-x}Fe_xO_3$ solid solutions with $0.0 \leq x \leq 0.4$. All the samples showed comparable enthalpies (about 7.0–7.9 J/g) of the structural phase transition (Figure 3). However, a systematic increase in enthalpy with increasing x can be seen.

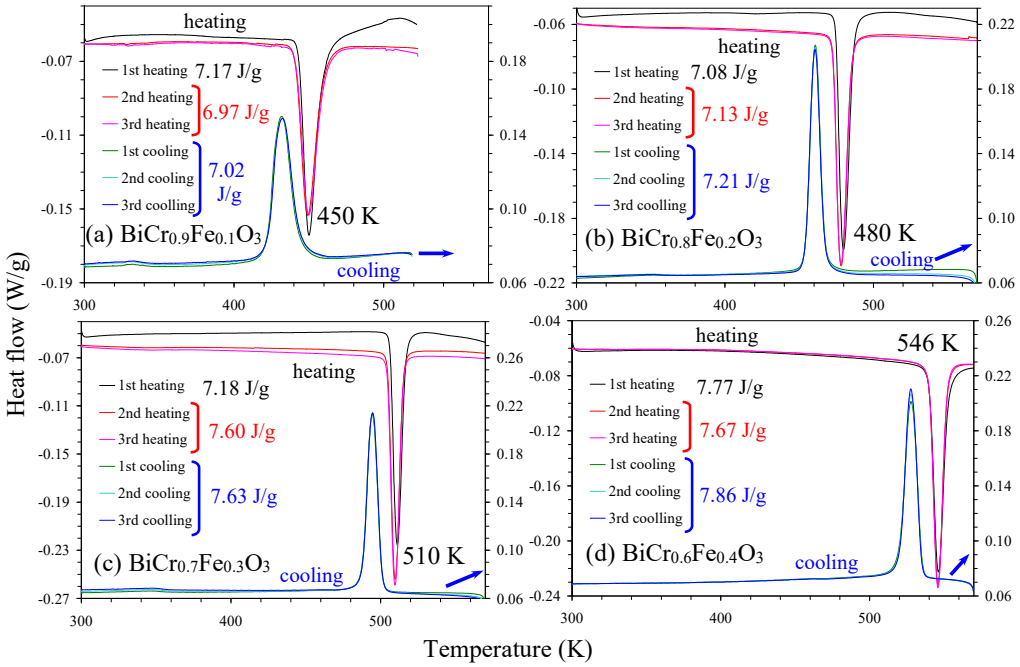

Figure 3. Differential scanning calorimetry (DSC) curves of (**a**) $BiCr_{0.9}Fe_{0.1}O_3$, (**b**) $BiCr_{0.8}Fe_{0.2}O_3$, (**c**) $BiCr_{0.7}Fe_{0.3}O_3$, and (**d**) $BiCr_{0.6}Fe_{0.4}O_3$ on heating (the left-hand axes) and cooling (the right-hand axes). Three DSC runs are given for each sample. Temperatures of peak positions on the heating curves are given. The peak areas (in J/g) are also given for the first heating curve, for the second and third heating curve (an average value), and for the first, second, and third cooling curves (an average value).

The *Pnma* modification of all the samples had sharp reflections without any anisotropic broadening or asymmetry. Therefore, structure parameters of the *Pnma* modifications could be readily refined from synchrotron XRD data. Refined structural parameters of the *Pnma* modifications for all the samples are summarized in Table 1, and Figure 4 shows fragments of experimental, calculated, and difference synchrotron XRPD data after the Rietveld fit at 550 K for the x = 0.1 sample as an example.

Figure 5 shows the compositional dependence of the lattice parameters and unit cell volume of the *Pnma* modifications at 550 K (Table S1 provides numerical data). Nearly linear increases in all parameters were observed with the increase in the Fe content in agreement with the larger ionic radius of Fe^{3+} cations (r_{VI} = 0.645 Å) in comparison to Cr^{3+} cations (r_{VI} = 0.615 Å) [67], confirming the formation of the solid solutions.

On the other hand, superstructure reflections of the $PbZrO_3$-type *Pbam* modifications in all the samples showed strong anisotropic broadening, and some reflections showed asymmetry from the high-angle side of the reflections (Figures 1 and 2 and Figure S1). For example (Figure 2b), the (021) reflection had the same width as the fundamental, main reflections, and it was symmetrical. The (111) reflection was very broad, and it was nearly symmetrical. The (110) reflection had intermediate broadening, and it showed asymmetry. Moreover, some reflections of the AP modification showed noticeable shifts from their expected, commensurate positions (for example, the (110), (130), and (210) reflections). Such shifts suggest the presence of incommensurate modulations. Such shifts were also present

in the HP modifications, but the shifts were less pronounced. Therefore, the presence of incommensurate modulations and significant anisotropic broadening prevented us from determining the precise structural parameters of the HP and AP modifications at RT.

Table 1. Structure parameters of $BiCr_{1-x}Fe_xO_3$ at high temperatures from synchrotron powder X-ray diffraction data.

x	0.1	0.2	0.3	0.4
T (K)	550	550	600	600
a (Å)	5.55595 (3)	5.56458 (3)	5.57383 (2)	5.58329 (2)
b (Å)	7.77499 (6)	7.78492 (6)	7.80159 (3)	7.81360 (3)
c (Å)	5.44100 (3)	5.44552 (3)	5.45751 (2)	5.46389 (2)
V (Å^3)	235.037 (3)	235.899 (3)	237.318 (2)	238.366 (2)
ρ_{cal} (g/cm^3)	8.743	8.721	8.680	8.653
x (Bi)	0.04309 (6)	0.04275 (8)	0.04304 (7)	0.04281 (8)
z (Bi)	0.99574 (14)	0.99616 (23)	0.99618 (18)	0.99613 (21)
B_{iso} (Bi) (Å^2)	1.173 (7)	1.364 (11)	1.528 (10)	1.643 (11)
B_{iso} (Cr/Fe) (Å^2)	0.55 (2)	0.72 (3)	0.76 (2)	0.79 (3)
x (O1)	0.4800 (9)	0.4871 (12)	0.4852 (11)	0.4860 (12)
z (O1)	0.0823 (10)	0.0747 (13)	0.0847 (12)	0.0824 (13)
B_{iso} (O1) (Å^2)	0.62 (13)	0.10 (17)	0.88 (16)	0.55 (18)
x (O2)	0.2915 (9)	0.2921 (15)	0.2945 (11)	0.2994 (13)
y (O2)	0.0385 (6)	0.0413 (11)	0.0374 (8)	0.0381 (10)
z (O2)	0.7068 (9)	0.7071 (15)	0.7030 (11)	0.7041 (13)
B_{iso} (O2) (Å^2)	1.06 (10)	2.4 (2)	1.51 (13)	1.97 (17)
R_{wp} (%)	5.48	7.18	6.39	7.09
R_p (%)	4.07	5.28	4.81	5.18
R_I (%)	3.18	4.17	4.26	4.16
R_F (%)	2.51	3.81	4.35	4.56
Impurities:				
$Bi_2O_2CO_3$	1.1 wt. %	0.8 wt. %	1.6 wt. %	1.6 wt. %
Cr_2O_3	0.6 wt. %	0.9 wt. %	–	–

Crystal system: orthorhombic. Space group: *Pnma* (No. 62); $Z = 4$. Source: synchrotron powder X-ray diffraction ($\lambda = 0.420138$ Å). d-space range used in the refinements: 0.497–11.563 Å. Fractional coordinates: Bi: 4*c* (x, 0.25, z), Cr/Fe: 4*b* (0, 0, 0.5), O1: 4*c* (x, 0.25, z), and O2: 8*d* (x, y, z). Occupation factors, g, of the Bi and O sites are 1. The occupation factor of the Cr/Fe site is mixed based on the nominal compositions.

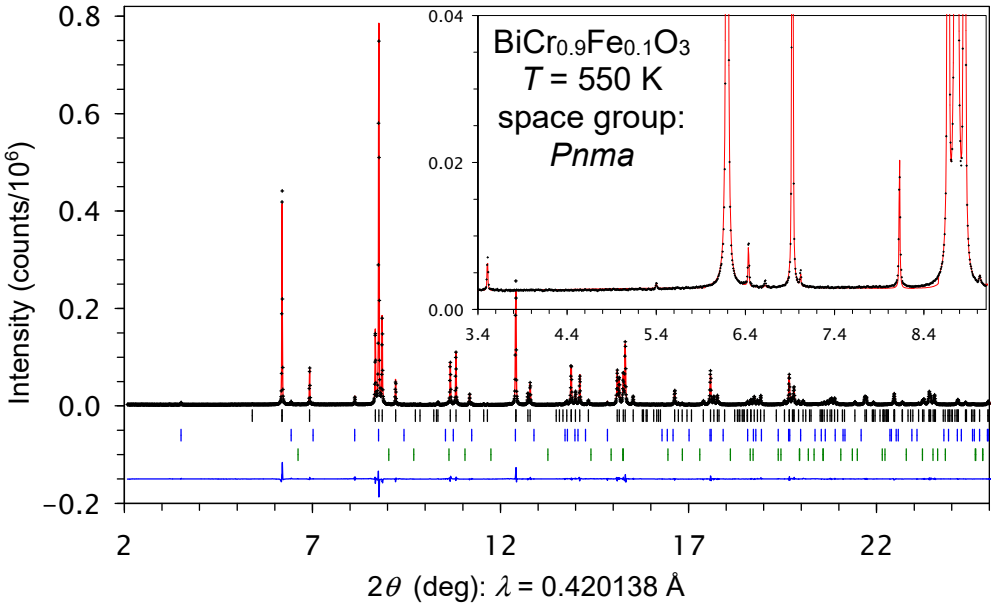

Figure 4. Fragments (between 2° and 25°) of experimental (black crosses), calculated (red line), and difference (blue line at the bottom) synchrotron powder X-ray diffraction patterns of $BiCr_{0.9}Fe_{0.1}O_3$ at $T = 550$ K in the *Pnma* modification. The tick marks show possible Bragg reflection positions for the main phase (black) and $Bi_2O_2CO_3$ (blue) and Cr_2O_3 (green) impurities from top to bottom. The inset shows a magnified fragment.

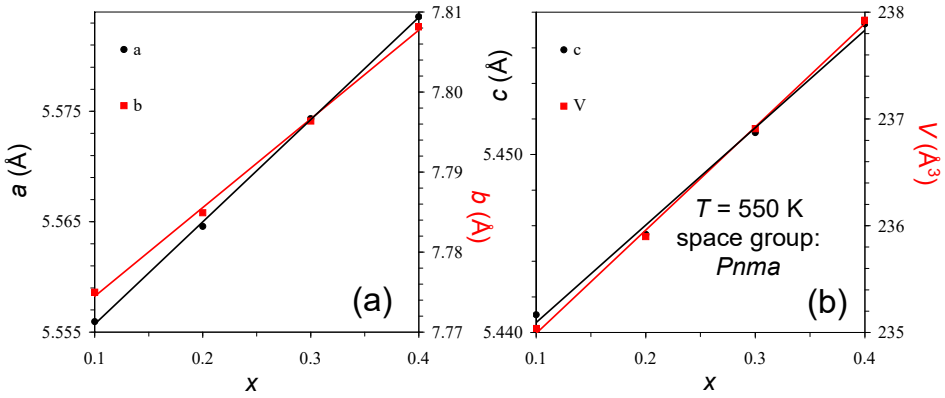

Figure 5. Compositional dependence of the lattice parameters of the *Pnma* modifications of the $BiCr_{1-x}Fe_xO_3$ solid solutions at T = 550 K. (**a**) The *a* and *b* lattice parameters, (**b**) the *c* lattice parameter and unit cell volume. Data on heating are used for x = 0.1, 0.2, and 0.3 and on cooling—for x = 0.4.

$BiFeO_3$ has an incommensurate AFM structure, but $BiFeO_3$ has a well-defined commensurate crystal structure [6]. Incommensurate structural modulations were only observed in the rare-earth-doped samples, $Bi_{1-x}R_xFeO_3$, where R^{3+} is a rare-earth element, and at very limited compositional regions [40,68–73]. To the best of our knowledge, incommensurate structural modulations found in $BiCr_{1-x}Fe_xO_3$ samples, especially in the AP modifications, have never been observed before in the only-transition-metal-doped $BiFe_{1-x}M_xO_3$, where M is a transition metal element. Electron diffraction will be essential to understand incommensurate structural modulations of $BiCr_{1-x}Fe_xO_3$ samples.

Figure 6a shows the temperature dependence of the lattice parameters of $BiCr_{0.6}Fe_{0.4}O_3$ on heating and cooling (Table S2 provides numerical data). Drastic changes in the fundamental perovskite reflections were observed during the transition from the *Pbam* modification to the *Pnma* modification. The unit cell volume also drops by −1.4% at 550 K, where the two phases coexist, suggesting the first-order structural phase transition. It is interesting that the *a* lattice parameter of the *Pnma* modification decreased with increasing temperature, suggesting anisotropic thermal expansion. All other parameters of the *Pnma* modification and all parameters of the *Pbam* modification increased with increasing temperature as expected. The fundamental lattice parameters of the HP and AP modifications were very close to each other at RT (Figure 6). However, the superstructure reflections were slightly different as discussed above. Therefore, we can discuss the different modifications, namely the HP and AP modifications, and the observation of the conversion polymorphism phenomenon [41] in the $BiCr_{1-x}Fe_xO_3$ system similar to the conversion polymorphism phenomenon in the $BiFe_{1-x}Sc_xO_3$ system [41] and the $BiFe_{1-x}Mn_xO_3$ system [36,49].

Because of the presence of some structural differences between the HP and AP modifications, we investigated the effects of the structural differences on the magnetic properties. Temperature-dependent magnetization curves of the HP and AP modifications are shown in Figures 7–10, and the results of M versus H measurements are shown in Figures 11–14 (Figures S2–S5 show magnified parts of Figures 11–14). The HP and AP modifications of $BiCr_{0.9}Fe_{0.1}O_3$ showed very similar magnetic properties with one detectable magnetic transition at T_N = 100 K despite their different phase compositions (a different ratio of the *Pbam* and *C*2/*c* phases). Undoped $BiCrO_3$ has T_N = 112 K and shows a spin reorientation transition at T_{N2} = 72 K [23]. No signs of a spin reorientation transition were found in $BiCr_{0.9}Fe_{0.1}O_3$. A noticeable weak FM moment appeared below T_N = 100 K at H = 100 Oe and H = 10 kOe (Figure 7). The transition with the weak FM moment with T_N = 100 K could correspond to the behavior of the *C*2/*c* phase. The *Pbam* phase has a much weaker FM moment (see properties of the x = 0.3 and 0.4 samples); therefore, its contribution to magnetic properties could be hidden in the x = 0.1 sample.

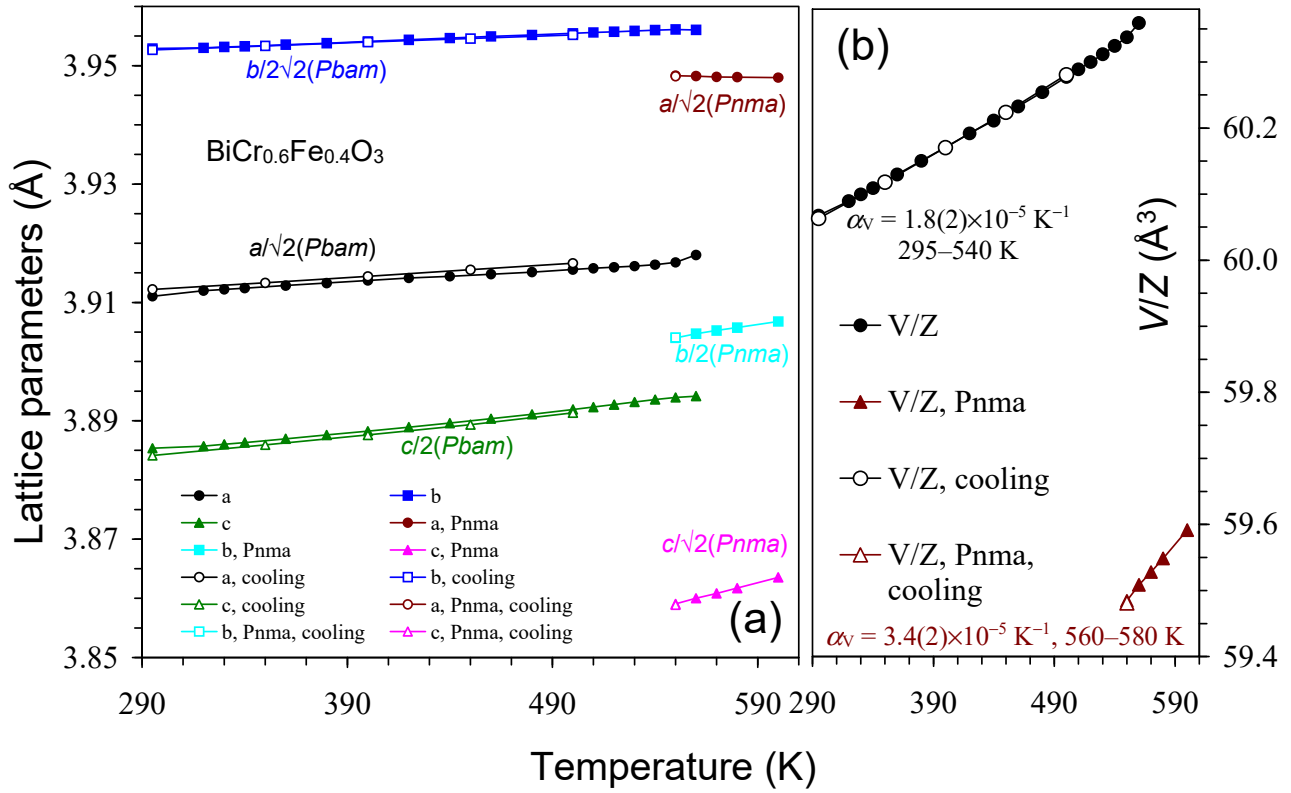

Figure 6. (**a**) The temperature dependence of the normalized lattice parameters of $BiCr_{0.6}Fe_{0.4}O_3$ on heating (full symbols) and cooling (empty symbols). (**b**) The temperature dependence of the normalized unit cell volumes (V/Z). α_V is the volumetric coefficient of thermal expansion.

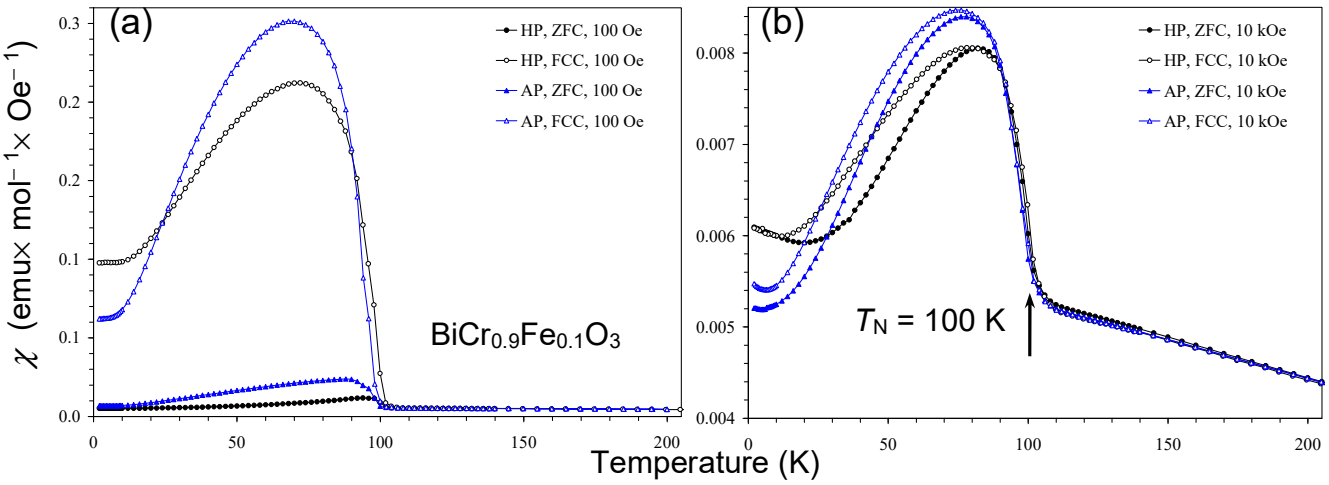

Figure 7. Magnetic properties of HP-$BiCr_{0.9}Fe_{0.1}O_3$ (circles) and AP-$BiCr_{0.9}Fe_{0.1}O_3$ (triangles). Zero-field-cooled (ZFC: filled curves) and field-cooled on cooling (FCC: empty curves) curves are shown at (**a**) H = 100 Oe and (**b**) H = 10 kOe.

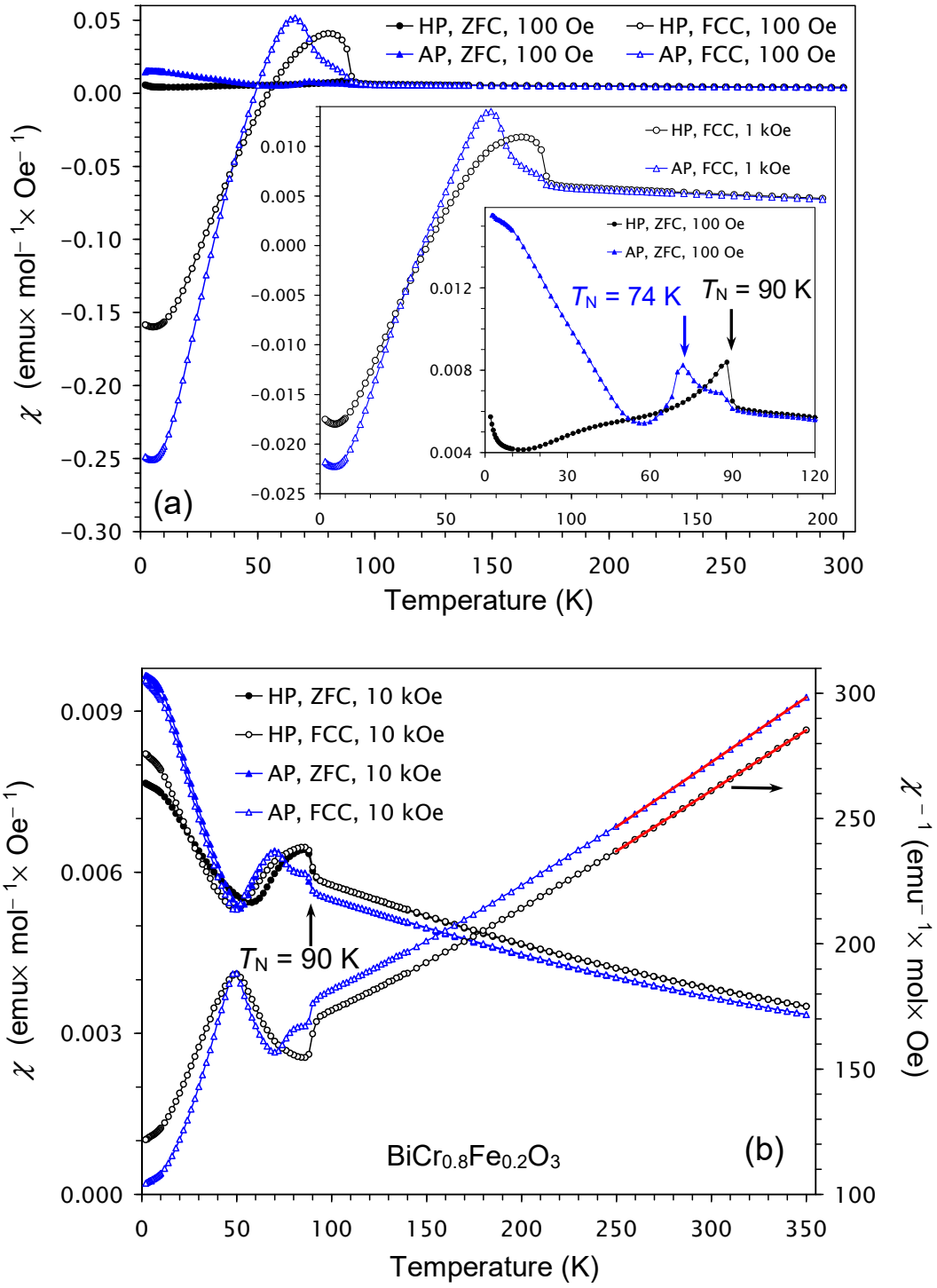

Figure 8. Magnetic properties of HP-$BiCr_{0.8}Fe_{0.2}O_3$ (circles) and AP-$BiCr_{0.8}Fe_{0.2}O_3$ (triangles). Zero-field-cooled (ZFC: filled curves) and field-cooled on cooling (FCC: empty curves) curves are shown at (**a**) H = 100 Oe and (**b**) H = 10 kOe. The main inset on panel (**a**) shows the FCC curves H = 1 kOe. The secondary inset shows the ZFC curves H = 100 Oe. The right-hand axis on panel (**b**) gives the inverse FCC χ^{-1} versus T curves at H = 10 kOe with Curie–Weiss fits (red lines).

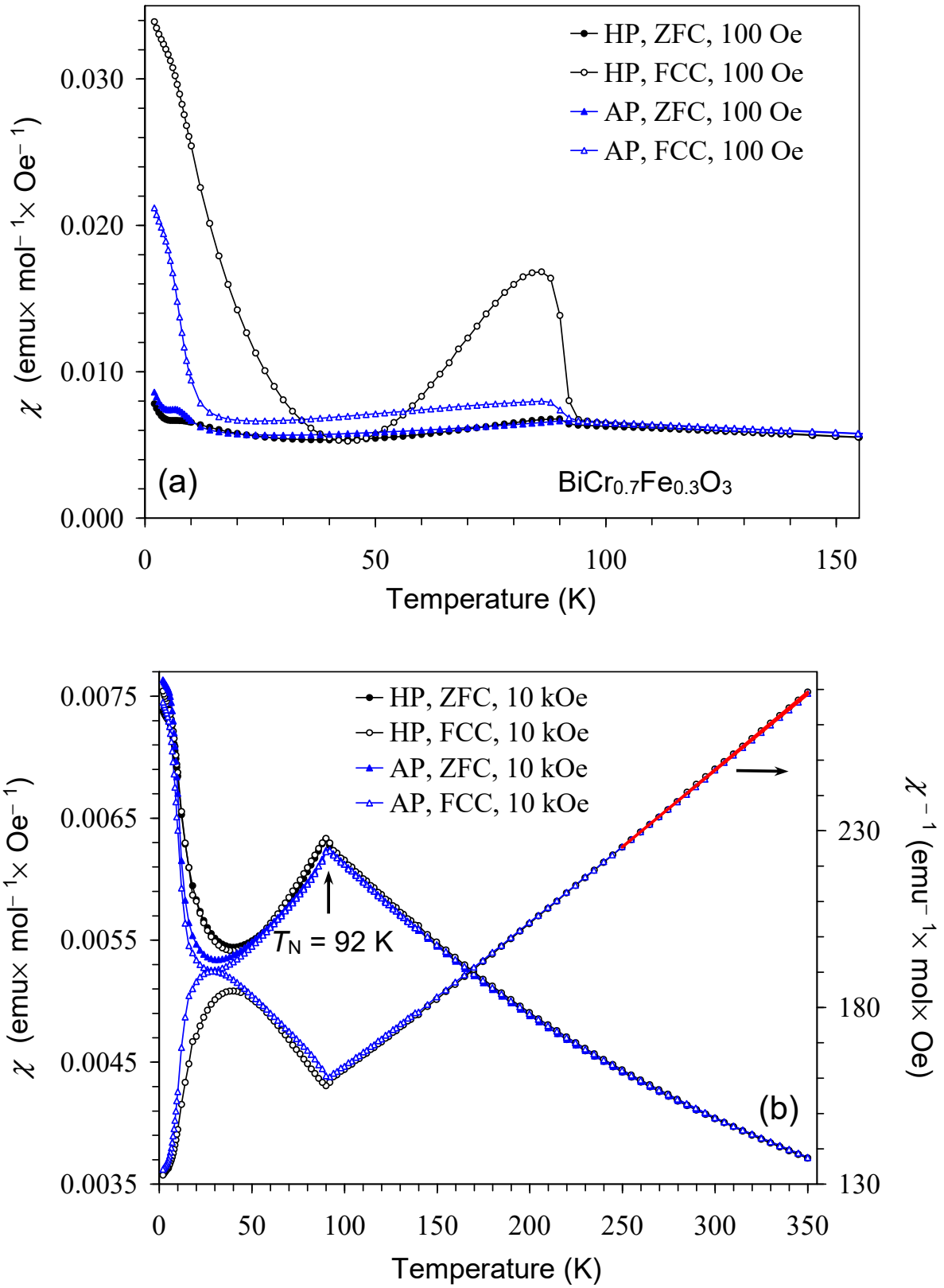

Figure 9. Magnetic properties of HP-$BiCr_{0.7}Fe_{0.3}O_3$ (circles) and AP-$BiCr_{0.7}Fe_{0.3}O_3$ (triangles). Zero-field-cooled (ZFC: filled curves) and field-cooled on cooling (FCC: empty curves) curves are shown at (**a**) H = 100 Oe and (**b**) H = 10 kOe. The right-hand axis on panel (**b**) gives the inverse FCC χ^{-1} versus T curves at H = 10 kOe with Curie–Weiss fits (red lines).

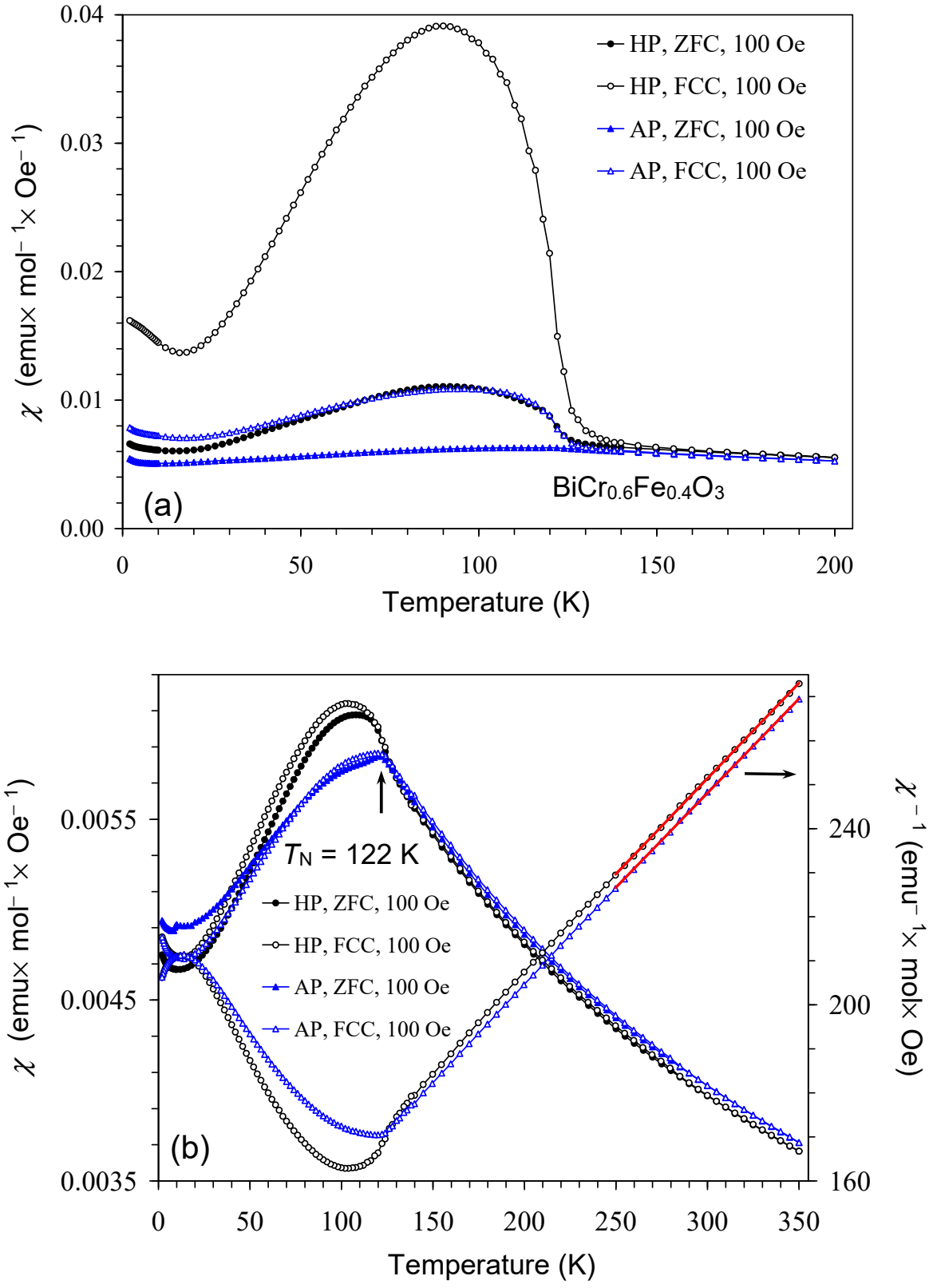

Figure 10. Magnetic properties of HP-$BiCr_{0.6}Fe_{0.4}O_3$ (circles) and AP-$BiCr_{0.6}Fe_{0.4}O_3$ (triangles). Zero-field-cooled (ZFC: filled curves) and field-cooled on cooling (FCC: empty curves) curves are shown at (**a**) H = 100 Oe and (**b**) H = 10 kOe. The right-hand axis on panel (**b**) gives the inverse FCC χ^{-1} versus T curves at H = 10 kOe with Curie–Weiss fits (red lines).

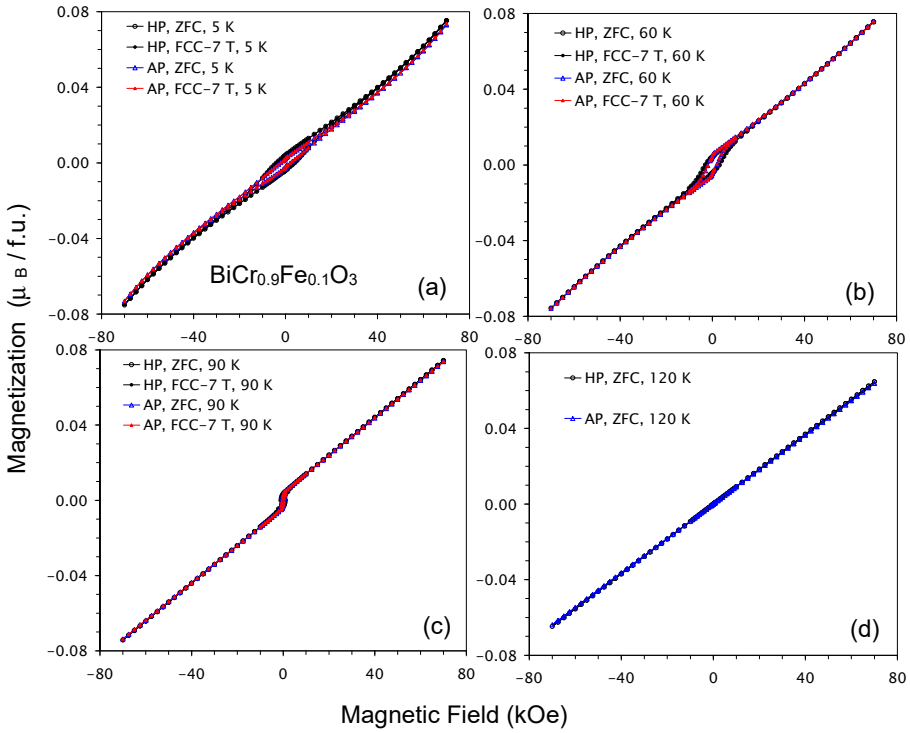

Figure 11. Comparison of magnetic properties of HP-$BiCr_{0.9}Fe_{0.1}O_3$ and AP-$BiCr_{0.9}Fe_{0.1}O_3$: *M* versus *H* curves at (**a**) *T* = 5 K, (**b**) *T* = 60 K, (**c**) *T* = 90 K, and (**d**) *T* = 120 K. *M* versus *H* curves are measured under the ZFC procedure, when samples are cooled from 300 K to measurement temperatures under *H* = 0 Oe, and under the FCC procedure (marked as FCC–7 T), when samples are cooled from 300 K to measurement temperatures under *H* = 70 kOe.

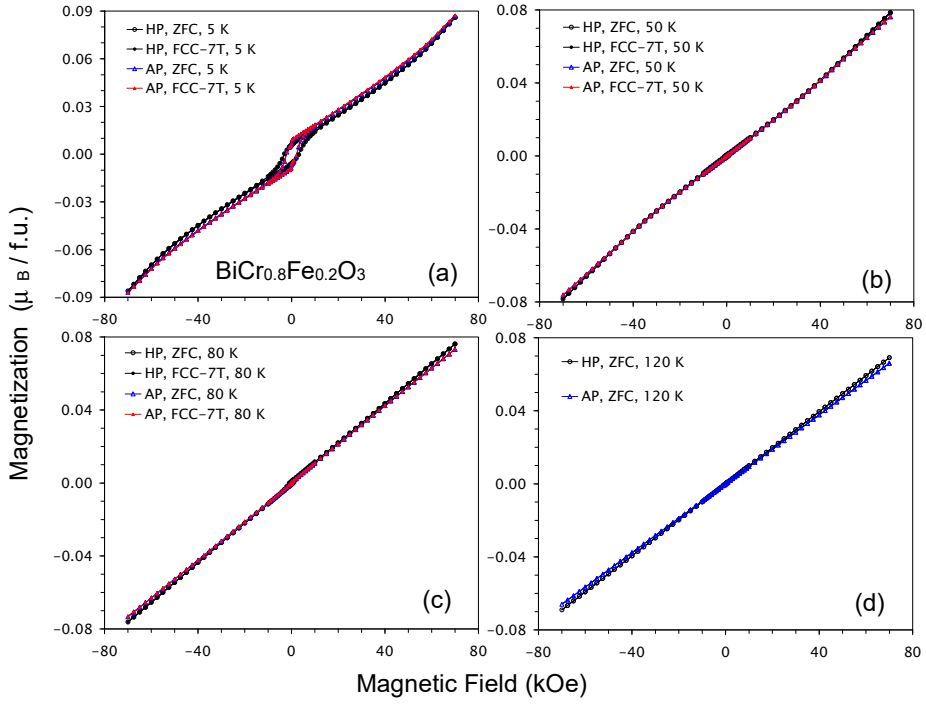

Figure 12. Comparison of magnetic properties of HP-$BiCr_{0.8}Fe_{0.2}O_3$ and AP-$BiCr_{0.8}Fe_{0.2}O_3$: *M* versus *H* curves at (**a**) *T* = 5 K, (**b**) *T* = 50 K, (**c**) *T* = 80 K, and (**d**) *T* = 120 K. *M* versus *H* curves were measured under the ZFC procedure, when samples are cooled from 300 K to measurement temperatures under *H* = 0 Oe, and under the FCC procedure (marked as FCC–7 T), when samples are cooled from 300 K to measurement temperatures under *H* = 70 kOe.

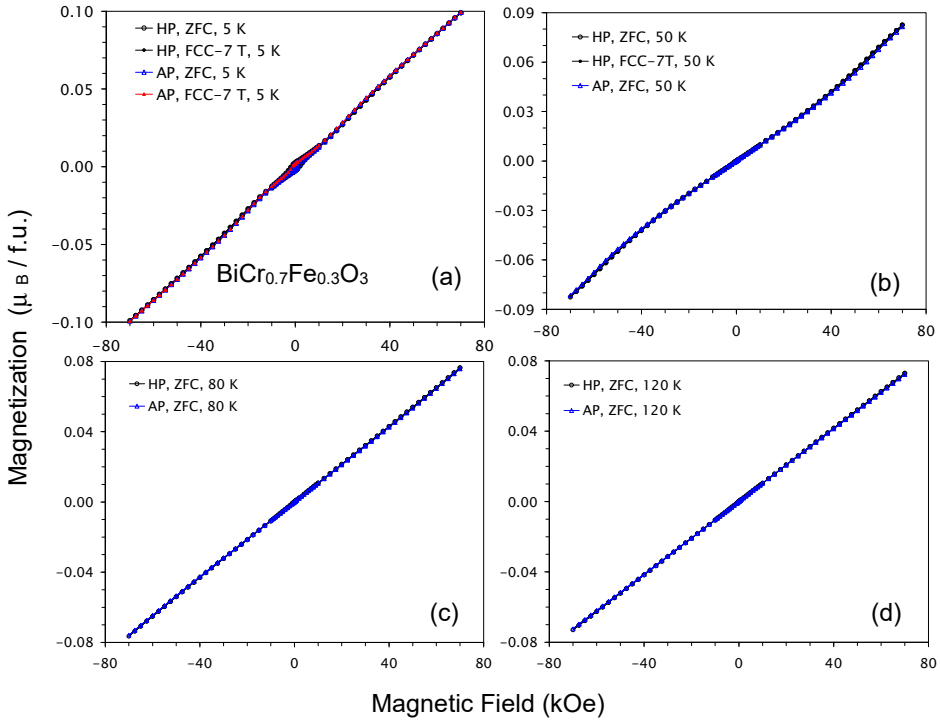

Figure 13. Comparison of magnetic properties of HP-$BiCr_{0.7}Fe_{0.3}O_3$ and AP-$BiCr_{0.7}Fe_{0.3}O_3$: *M* versus *H* curves at (**a**) *T* = 5 K, (**b**) *T* = 50 K, (**c**) *T* = 80 K, and (**d**) *T* = 120 K. *M* versus *H* curves are measured under the ZFC procedure, when samples are cooled from 300 K to measurement temperatures under *H* = 0 Oe, and under the FCC procedure (marked as FCC–7 T), when samples are cooled from 300 K to measurement temperatures under *H* = 70 kOe.

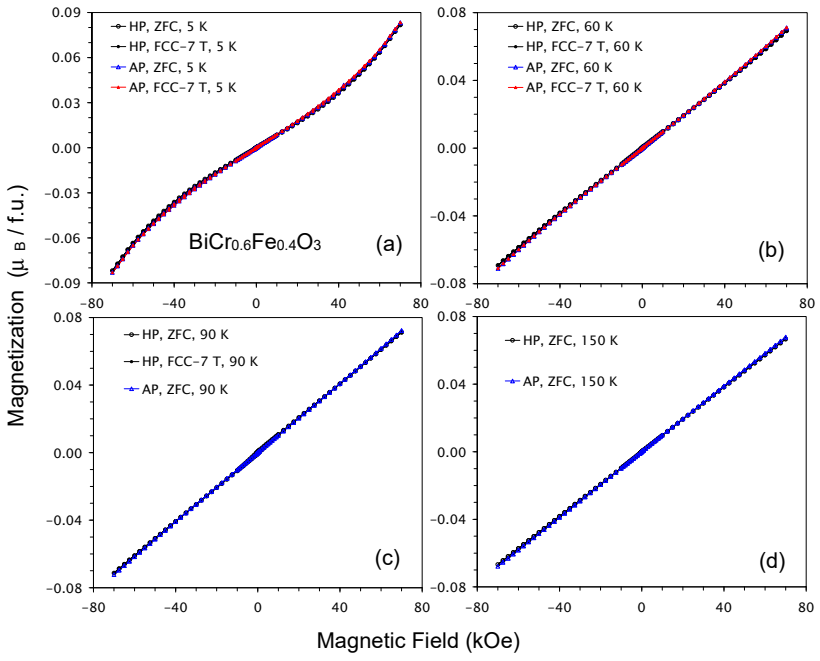

Figure 14. Comparison of magnetic properties of HP-$BiCr_{0.6}Fe_{0.4}O_3$ and AP-$BiCr_{0.6}Fe_{0.4}O_3$: *M* versus *H* curves at (**a**) *T* = 5 K, (**b**) *T* = 60 K, (**c**) *T* = 90 K, and (**d**) *T* = 150 K. *M* versus *H* curves are measured under the ZFC procedure, when samples are cooled from 300 K to measurement temperatures under *H* = 0 Oe, and under the FCC procedure (marked as FCC–7 T), when samples are cooled from 300 K to measurement temperatures under *H* = 70 kOe.

HP-$BiCr_{0.8}Fe_{0.2}O_3$ clearly showed one transition at T_N = 90 K (Figure 8) because of the relatively large fraction of the *C*2/*c* phase. On the other hand, AP-$BiCr_{0.8}Fe_{0.2}O_3$ clearly

showed two transitions, the first one at T_N = 90 K from traces of the *C*2/*c* phase and the second one at T_N = 74 K from the majority of the *Pbam* phase. Traces of the *C*2/*c* phase could still be detected as this phase had a much larger FM moment. It is interesting that both HP- and AP-$BiCr_{0.8}Fe_{0.2}O_3$ showed a negative magnetization phenomenon [74] when the FCC curves were measured at H = 100 Oe and 1 kOe. Negative magnetization phenomena are often observed in different $RCr_{1-x}Fe_xO_3$ or $RFe_{1-x}Cr_xO_3$ solid solutions, where R^{3+} is a rare-earth element [75,76].

The magnetic properties of both HP- and AP-$BiCr_{0.7}Fe_{0.3}O_3$ were nearly identical when measured at high magnetic fields, such as *H* = 10 kOe (Figure 9b), with one AFM-like anomaly at T_N = 92 K. A very weak FM contribution (from spin canting) started emerging below about 20 K (Figures 9b and 13a). An extremely weak FM contribution also appeared just below T_N = 92 K at weak magnetic fields, such as *H* = 100 Oe (Figure 9a), and HP-$BiCr_{0.7}Fe_{0.3}O_3$ had a larger FM contribution in comparison to AP-$BiCr_{0.7}Fe_{0.3}O_3$. The weak FM contribution in HP- and AP-$BiCr_{0.7}Fe_{0.3}O_3$ at *H* = 100 Oe was about 10 times smaller than that of HP- and AP-$BiCr_{0.9}Fe_{0.1}O_3$.

Magnetic properties of both HP- and AP-$BiCr_{0.6}Fe_{0.4}O_3$ were nearly identical when measured at high magnetic fields, such as *H* = 10 kOe (Figure 10b), with one AFM-like anomaly at T_N = 122 K. No weak FM contributions appeared at lower temperatures in comparison with HP- and AP-$BiCr_{0.7}Fe_{0.3}O_3$ at *H* = 10 kOe. At a small magnetic field of H = 100 Oe, HP-$BiCr_{0.6}Fe_{0.4}O_3$ had a larger FM contribution in comparison to AP-$BiCr_{0.6}Fe_{0.4}O_3$. However, the weak FM contributions were extremely small, meaning that they could not be detected on the *M* versus *H* curves, which showed linear behavior in the vicinity of the origin between about −20 kOe and 20 kOe (Figure 14).

At high temperatures, inverse magnetic susceptibilities follow the Curie–Weiss law for all the samples (Figures 8b, 9b and 10b), and parameters of the Curie–Weiss fits are summarized in Table 2. The experimental effective magnetic moments were close to the expected, calculated ones. The Weiss temperature varied between −230 K and −280 K, resulting in a moderate frustration index of about 2.3 to 2.9. It is interesting that some *M* versus *H* curves showed noticeable upturn deviations from the linear behavior (at high magnetic fields), suggesting the presence of gradual field-induced transitions, for example, at *T* = 5 K for *x* = 0.4 (Figure 14a), *T* = 50 K for *x* = 0.3 (Figure 13b), *T* = 5 K and 50 K for *x* = 0.2 (Figure 12a,b), and *T* = 5 K for *x* = 0.1 (Figure 11a).

Table 2. Temperatures of structural transitions (T_{str}) and magnetic anomalies (T_N) and parameters of the Curie–Weiss fits and *M* versus *H* curves at *T* = 5 K for $BiCr_{1-x}Fe_xO_3$.

x	T_{str} (K)	T_N (K)	μ_{eff} (μ_B/f.u.)	μ_{calc} (μ_B/f.u.)	θ (K)	M_S (μ_B/f.u.)
0.1 (HP)	450	100	3.995	4.123	−247	0.075
0.1 (AP)	450	98	4.061	4.123	−259	0.073
0.2 (HP)	480	90	4.068	4.359	−240	0.086
0.2 (AP)	478	90, 74	3.934	4.359	−227	0.087
0.3 (HP)	511	92	4.269	4.583	−264	0.099
0.3 (AP)	510	92	4.305	4.583	−273	0.099
0.4 (HP)	546	122	4.293	4.796	−279	0.083
0.4 (AP)	546	122	4.321	4.796	−279	0.083

The Curie–Weiss fits are performed between 250 and 350 K using the FCC χ^{-1} versus *T* data at 10 kOe. M_S is the magnetization value at *T* = 5 K and *H* = 70 kOe. μ_{calc} is calculated using $5.916\mu_B$ for Fe^{3+} and $3.873\mu_B$ for Cr^{3+}. T_N values are determined from peaks on the 100 Oe FCC $d(\chi T)/dT$ versus *T* curves. T_{str} values are determined from peak positions on the heating DSC curves, where the anomalies on the first heating curves are assigned to the HP modification and the anomalies on the second and third heating curves are assigned to the AP modification. T_{str} corresponds to a transition to the $GdFeO_3$-type *Pnma* modification.

Figure 15 summarizes the temperature–composition phase diagram of the $BiCr_{1-x}Fe_xO_3$ system using the results of the current study and the literature data for the $BiFeO_3$ [6], $BiCrO_3$ [23,24,31], and $BiCr_{1-x}Fe_xO_3$ systems with high Fe content [63]. On the scale of Figure 15, T_N remains nearly the same for $0.0 \leq x \leq 0.4$ and then monotonically increases from $x = 0.4$ to $x = 1$. T_{str} increases gradually for $0.0 \leq x \leq 0.4$ and then more rapidly from $x = 0.4$ to $x = 1$.

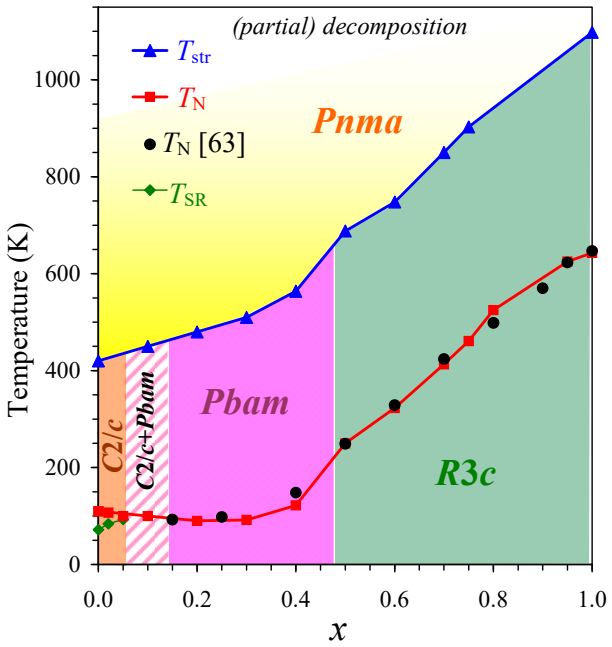

Figure 15. The temperature–composition phase diagram of the $BiCr_{1-x}Fe_xO_3$ system. T_{str} is the temperature of the structural transition to the *Pnma* modification. T_N is the Néel temperature. T_{SR} is the temperature of the spin reorientation transition.

3. Materials and Methods

The as-synthesized HP modifications of $BiCr_{1-x}Fe_xO_3$ solid solutions with $x = 0.1$, 0.2, 0.3, and 0.4 were prepared from stoichiometric mixtures of Bi_2O_3 (Rare Metallic Co., Tokyo, Japan, 99.9999%), Fe_2O_3 (Rare Metallic Co., Tokyo, Japan, 99.999%), and Cr_2O_3 (Rare Metallic Co., Tokyo, Japan, 99.9%). The synthesis was performed at about 6 GPa and about 1600 K for 1 h in sealed Pt capsules using a belt-type HP instrument. After annealing at 1600 K, the samples were cooled down to room temperature by turning off the heating current, and the pressure was slowly released. The AP modifications of $BiCr_{1-x}Fe_xO_3$ solid solutions with $x = 0.1$, 0.2, 0.3, and 0.4 were obtained by heating HP-$BiCr_{1-x}Fe_xO_3$ in air at AP at 623 K for 10 min (with a heating/cooling rate of 10 K/min). We note that at $x \geq 0.5$, a different modification with space group *R3c* is formed [62] (that is confirmed by us); therefore, compositions with $x \geq 0.5$ were not included in the present work.

X-ray powder diffraction (XRPD) data were collected at room temperature on a MiniFlex600 diffractometer (Rigaku, Tokyo, Japan) using CuKα radiation (2θ range of 8–100°, a step width of 0.02°, and scan speed of 2 °/min). Synchrotron XRPD data of HP-$BiCr_{1-x}Fe_xO_3$ were collected at 297 K, upon heating to 550 K ($x = 0.1$ and 0.2) or to 600 K ($x = 0.3$ and 0.4), and then on cooling to 297 K using the beamline BL02B2 [77,78] of SPring-8, Japan. Intensity data were taken between 2.082° and 78.216° at a 0.006° interval in 2θ using a wavelength of $\lambda = 0.420138$ Å; however, data up to 50° were used in the Rietveld analysis as no detectable experimental reflections were observed above 50°. The measurement time was 300 s at 297 K and 550 K (or 600 K) and 60 s at other temperatures. The samples were placed into open Lindemann glass capillary tubes (with an inner diameter of 0.1 mm),

which were rotated during the measurements. The Rietveld analysis of all XRPD data was performed using the *RIETAN-2000* program [79]. The reported weight fractions of all the phases were calculated by the *RIETAN-2000* program [79] from the refined scale factors.

Magnetic measurements were performed on a SQUID magnetometer (Quantum Design MPMS3, San Diego, CA, USA) between 2 and 350 K in different applied fields using zero-field-cooled (ZFC) and field-cooled on cooling (FCC) procedures. Isothermal magnetization measurements, M versus H, were performed from 70 kOe to −70 kOe and from −70 kOe to 70 kOe using both ZFC and FCC procedures. In the ZFC procedure for M versus H measurements, the samples were cooled from 300 K to a measurement temperature under a zero magnetic field; in the FCC procedure, the samples were cooled from 300 K to a measurement temperature under a magnetic field of 70 kOe. The ZFC and FCC procedures for M versus H measurements were used to check the presence or absence of the exchange bias effect; no detectable difference was observed on M versus H curves measured in the ZFC and FCC procedures, suggesting the absence of the exchange bias effect.

Pieces of pellets were used in magnetic measurements. A pellet of each HP-$BiCr_{1-x}Fe_xO_3$ was first used to obtain magnetic properties of the HP modification; the same pellet was then transformed to AP-$BiCr_{1-x}Fe_xO_3$ as described above, and it was used in magnetic measurements to obtain magnetic properties of the AP modification.

Differential scanning calorimetry (DSC) curves of powder samples of HP-$BiCr_{1-x}Fe_xO_3$ were recorded on a Mettler Toledo DSC1 STAR^e system between 297 K and maximum 573 K in open Al capsules with a heating/cooling rate of 10 K/min. Three DSC runs were performed to check the reproducibility.

4. Conclusions

In conclusion, two modifications of the $BiCr_{1-x}Fe_xO_3$ perovskite solid solutions were prepared. The HP modifications (as-synthesized) were prepared by a high-pressure high-temperature method at 6 GPa. The AP modifications were obtained using a "conversion polymorphism" strategy after heating at AP above structural phase transition temperatures and cooling to room temperature. The HP and AP modifications had subtle structural differences and showed incommensurate structural modulations. Structural phase transitions to the *Pnma* modification were observed in all the samples and investigated in details. Subtle differences in magnetic properties of the HP and AP modifications were investigated and reported. In particular, the x = 0.2 samples demonstrated negative magnetization phenomena.

Supplementary Materials: The following supporting information can be downloaded at: https://www.mdpi.com/article/10.3390/inorganics13030091/s1, Figure S1: Fragments (between 4.4° and 7.4°) of experimental and calculated synchrotron powder X-ray diffraction patterns of HP-$BiCr_{0.6}Fe_{0.4}O_3$ and AP-$BiCr_{0.6}Fe_{0.4}O_3$ at T = 297 K; Figure S2: A magnified part of Figure 11; Figure S3: A magnified part of Figure 12; Figure S4: A magnified part of Figure 13; Figure S5: A magnified part of Figure 14; Table S1: Numerical data used to plot Figure 5; Table S2: Numerical data used to plot Figure 6.

Funding: This research received no external funding.

Institutional Review Board Statement: Not applicable.

Informed Consent Statement: Not applicable.

Data Availability Statement: The raw data supporting the conclusions of this article will be made available by the author on request.

Acknowledgments: Synchrotron radiation was used at the powder diffraction beamline BL02B2 at SPring-8, with permission from the Japan Synchrotron Radiation Research Institute (Proposal

Number: 2021A1334). The author thanks S. Kobayashi for his help at BL02B2 of SPring-8 and I.S. Soboleva for her preliminary studies of the $BiCr_{1-x}Fe_xO_3$ system. MANA was supported by the World Premier International Research Center Initiative (WPI), MEXT, Japan.

Conflicts of Interest: The author declares no conflicts of interest.

References

1. Venevtsev, Y.N.; Zhdanov, G.S.; Solov'ev, S.N.; Bezus, E.V.; Ivanova, V.V.; Fedulov, S.A.; Kapyshev, A.G. Crystal chemical studies of substances with perovskite structure and special dielectric properties. *Sov. Phys. Crystallogr.* **1961**, *5*, 594–599.
2. Filip'ev, V.S.; Smolyaninov, N.P.; Fesenko, E.G.; Belyaev, I.N. Synthesis of $BiFeO_3$ and determination of the unit cell. *Sov. Phys. Crystallogr.* **1961**, *5*, 913–914.
3. Zaslavskii, A.I.; Tutov, A.G. The structure of a new antiferromagnetic, $BiFeO_3$. *Dokl. Akad. Nauk SSSR* **1960**, *135*, 815–819.
4. Fedulov, S.A. Determination of Curie temperature for $BiFeO_3$ ferroelectric. *Dokl. Akad. Nauk SSSR* **1961**, *139*, 1345.
5. Wang, J.; Neaton, J.B.; Zheng, H.; Nagarajan, V.; Ogale, S.B.; Liu, B.; Viehland, D.; Vaithyanathan, V.; Schlom, D.G.; Waghmare, U.V.; et al. Epitaxial $BiFeO_3$ multiferroic thin film heterostructures. *Science* **2003**, *299*, 1719–1722. [CrossRef]
6. Catalan, G.; Scott, J.F. Physics and applications of bismuth ferrite. *Adv. Mater.* **2009**, *21*, 2463–2485. [CrossRef]
7. Khomskii, D. Classifying multiferroics: Mechanisms and effects. *Physics* **2009**, *2*, 20. [CrossRef]
8. Fiebig, M.; Lottermoser, T.; Meier, D.; Trassin, M. The evolution of multiferroics. *Nat. Rev. Mater.* **2016**, *1*, 16046. [CrossRef]
9. Tokura, Y.; Seki, S.; Nagaosa, N. Multiferroics of spin origin. *Rep. Prog. Phys.* **2014**, *77*, 076501. [CrossRef]
10. Meisenheimer, P.; Moore, G.; Zhou, S.; Zhang, H.; Huang, X.; Husain, S.; Chen, X.; Martin, L.W.; Persson, K.A.; Griffin, S.; et al. Switching the spin cycloid in $BiFeO_3$ with an electric field. *Nat. Comm.* **2024**, *15*, 2903. [CrossRef]
11. Liu, Z.R.; Wang, H.; Li, M.; Tao, L.L.; Paudel, T.R.; Yu, H.Y.; Wang, Y.X.; Hong, S.Y.; Zhang, M.; Ren, Z.H.; et al. In-plane charged domain walls with memristive behaviour in a ferroelectric film. *Nature* **2023**, *613*, 656–661. [CrossRef] [PubMed]
12. Paull, O.; Xu, C.S.; Cheng, X.; Zhang, Y.Y.; Xu, B.; Kelley, K.P.; de Marco, A.; Vasudevan, R.K.; Bellaiche, L.; Nagarajan, V.; et al. Anisotropic epitaxial stabilization of a low-symmetry ferroelectric with enhanced electromechanical response. *Nat. Mater.* **2022**, *21*, 74–80. [CrossRef] [PubMed]
13. Geng, W.R.; Zhu, Y.L.; Zhu, M.X.; Tang, Y.L.; Zhao, H.J.; Lei, C.H.; Wang, Y.J.; Wang, J.H.; Jiang, R.J.; Liu, S.Z.; et al. Dipolar wavevector interference induces a polar skyrmion lattice in strained $BiFeO_3$ films. *Nat. Nanotechnol.* **2025**. [CrossRef] [PubMed]
14. Huang, X.; Chen, X.; Li, Y.; Mangeri, J.; Zhang, H.; Ramesh, M.; Taghinejad, H.; Meisenheimer, P.; Caretta, L.; Susarla, S.; et al. Manipulating chiral spin transport with ferroelectric polarization. *Nat. Mater.* **2024**, *23*, 898–904. [CrossRef]
15. Arnold, D.C.; Knight, K.S.; Morrison, F.D.; Lightfoot, P. Ferroelectric-paraelectric transition in $BiFeO_3$: Crystal structure of the orthorhombic β phase. *Phys. Rev. Lett.* **2009**, *102*, 027602. [CrossRef]
16. Sugawara, F.; Iida, S.; Syono, Y.; Akimoto, S.-I. New magnetic perovskites $BiMnO_3$ and $BiCrO_3$. *J. Phys. Soc. Jpn.* **1965**, *20*, 1529. [CrossRef]
17. Tomashpol'skii, Y.Y.; Zubova, E.V.; Burdina, K.P.; Venevtsev, Y.N. X-ray diffraction study of the ferroelectric and ferromagnetic materials $BiMnO_3$, $BiCrO_3$, and their solid solutions obtained at high pressures. *Inorg. Mater.* **1967**, *3*, 1861–1863.
18. Sugawara, F.; Iiida, S.; Syono, Y.; Akimoto, S.-I. Magnetic properties and crystal distortions of $BiMnO_3$ and $BiCrO_3$. *J. Phys. Soc. Jpn.* **1968**, *25*, 1553–1558. [CrossRef]
19. Hill, N.A.; Bättig, P.; Daul, C. First principles search for multiferroism in $BiCrO_3$. *J. Phys. Chem. B* **2002**, *106*, 3383–3388. [CrossRef]
20. Niitaka, S.; Azuma, M.; Takano, M.; Nishibori, E.; Takata, M.; Sakata, M. Crystal structure and dielectric and magnetic properties of $BiCrO_3$ as a ferroelectromagnet. *Solid State Ion.* **2004**, *172*, 557–559. [CrossRef]
21. Murakami, M.; Fujino, S.; Lim, S.-H.; Long, C.J.; Salamanca-Riba, L.G.; Wuttig, M.; Takeuchi, I.; Nagarajan, V.; Varatharajan, A. Fabrication of multiferroic epitaxial $BiCrO_3$ thin films. *Appl. Phys. Lett.* **2006**, *88*, 152902. [CrossRef]
22. Kim, D.H.; Lee, H.N.; Varela, M.; Christen, H.M. Antiferroelectricity in multiferroic $BiCrO_3$ epitaxial films. *Appl. Phys. Lett.* **2006**, *89*, 162904. [CrossRef]
23. Belik, A.A.; Tsujii, N.; Suzuki, H.; Takayama-Muromachi, E. Magnetic properties of bulk $BiCrO_3$ studied with dc and ac magnetization and specific heat. *Inorg. Chem.* **2007**, *46*, 8746–8751. [CrossRef] [PubMed]
24. Belik, A.A.; Iikubo, S.; Kodama, K.; Igawa, N.; Shamoto, S.; Takayama-Muromachi, E. Neutron powder diffraction study on the crystal and magnetic structures of $BiCrO_3$. *Chem. Mater.* **2008**, *20*, 3765–3769. [CrossRef]
25. Darie, C.; Goujon, C.; Bacia, M.; Klein, H.; Toulemonde, P.; Bordet, P.; Suard, E. Magnetic and crystal structures of $BiCrO_3$. *Solid State Sci.* **2010**, *12*, 660–664. [CrossRef]
26. Colin, C.V.; Pérez, A.G.; Bordet, P.; Goujon, C.; Darie, C. Symmetry adapted analysis of the magnetic and structural phase diagram of $Bi_{1-x}Y_xCrO_3$. *Phys. Rev. B* **2012**, *85*, 224103. [CrossRef]
27. Singh, A.; Singh, V.N.; Canadell, E.; Íñiguez, J.; Diéguez, O. Polymorphism in Bi-based perovskite oxides: A first-principles study. *Phys. Rev. Mater.* **2018**, *2*, 104417. [CrossRef]

28. Sobolev, A.V.; Bokov, A.V.; Yi, W.; Belik, A.A.; Presniakov, I.A.; Glazkova, I.S. Electric hyperfine interactions of ^{57}Fe impurity atoms in $ACrO_3$ perovskite-type chromites (A = Sc, In, Tl, Bi). *J. Exp. Theor. Phys.* **2019**, *129*, 896–902. [CrossRef]
29. Araújo, B.S.; Arévalo-López, A.M.; Santos, C.C.; Attfield, J.P.; Paschoal, C.W.A.; Ayala, A.P. Spin–phonon coupling in monoclinic $BiCrO_3$. *J. Appl. Phys.* **2020**, *127*, 114102. [CrossRef]
30. Cardoso, J.P.; Delmonte, D.; Gilioli, E.; Fertman, E.L.; Fedorchenko, A.V.; Shvartsman, V.V.; Paukšta, V.; Grigalaitis, R.; Banys, J.; Khalyavin, D.D.; et al. Phase transitions in the metastable perovskite multiferroics $BiCrO_3$ and $BiCr_{0.9}Sc_{0.1}O_3$: A comparative study. *Inorg. Chem.* **2020**, *59*, 8727–8735. [CrossRef]
31. Behr, D.; Delmonte, D.; Gilioli, E.; Khalyavin, D.D.; Johnson, R.D. Weak ferromagnetism and spin reorientation in antiferroelectric $BiCrO_3$. *Phys. Rev. B* **2022**, *106*, 024416. [CrossRef]
32. Belik, A.A. Polar and nonpolar phases of BiMO_3: A review. *J. Solid State Chem.* **2012**, *195*, 32–40. [CrossRef]
33. Selbach, S.M.; Tybell, T.; Einarsrud, M.A.; Grande, T. Structure and properties of multiferroic oxygen hyperstoichiometric $BiFe_{1-x}Mn_xO_{3+\delta}$. *Chem. Mater.* **2009**, *21*, 5176–5186. [CrossRef]
34. Selbach, S.M.; Tybell, T.; Einarsrud, M.A.; Grande, T. High-temperature semiconducting cubic phase of $BiFe_{0.7}Mn_{0.3}O_{3+\delta}$. *Phys. Rev. B* **2009**, *79*, 214113. [CrossRef]
35. Mandal, P.; Sundaresan, A.; Rao, C.N.R.; Iyo, A.; Shirage, P.M.; Tanaka, Y.; Simon, C.; Pralong, V.; Lebedev, O.I.; Caignaert, V.; et al. Temperature-induced magnetization reversal in $BiFe_{0.5}Mn_{0.5}O_3$ synthesized at high pressure. *Phys. Rev. B* **2010**, *82*, 100416. [CrossRef]
36. Karpinsky, D.V.; Silibin, M.V.; Latushka, S.I.; Zhaludkevich, D.V.; Sikolenko, V.V.; Svetogorov, R.; Sayyed, M.I.; Almousa, N.; Trukhanov, A.; Trukhanov, S.; et al. Temperature-driven transformation of the crystal and magnetic structures of $BiFe_{0.7}Mn_{0.3}O_3$ ceramics. *Nanomaterials* **2022**, *12*, 2813. [CrossRef]
37. Manna, P.K.; Yusuf, S.M.; Shukla, R.; Tyagi, A.K. Exchange bias in $BiFe_{0.8}Mn_{0.2}O_3$ nanoparticles with an antiferromagnetic core and a diluted antiferromagnetic shell. *Phys. Rev. B* **2011**, *83*, 184412. [CrossRef]
38. Khalyavin, D.D.; Salak, A.N.; Olekhnovich, N.M.; Pushkarev, A.V.; Radyush, Y.V.; Manuel, P.; Raevski, I.P.; Zheludkevich, M.L.; Ferreira, M.G.S. Polar and antipolar polymorphs of metastable perovskite $BiFe_{0.5}Sc_{0.5}O_3$. *Phys. Rev. B* **2014**, *89*, 174414. [CrossRef]
39. Salak, A.N.; Khalyavin, D.D.; Pushkarev, A.V.; Radyush, Y.V.; Olekhnovich, N.M.; Shilin, A.D.; Rubanik, V.V. Phase formation in the (1-y)$BiFeO_3$-y$BiScO_3$ system under ambient and high pressure. *J. Solid State Chem.* **2017**, *247*, 90–96. [CrossRef]
40. Khalyavin, D.D.; Salak, A.N.; Lopes, A.B.; Olekhnovich, N.M.; Pushkarev, A.V.; Radyush, Y.V.; Fertman, E.L.; Desnenko, V.A.; Fedorchenko, A.V.; Manuel, P.; et al. Magnetic structure of an incommensurate phase of La-doped $BiFe_{0.5}Sc_{0.5}O_3$: Role of antisymmetric exchange interactions. *Phys. Rev. B* **2015**, *92*, 224428. [CrossRef]
41. Khalyavin, D.D.; Salak, A.N.; Fertman, E.L.; Kotlyar, O.V.; Eardley, E.; Olekhnovich, N.M.; Pushkarev, A.V.; Radyush, Y.V.; Fedorchenko, A.V.; Desnenko, V.A.; et al. The phenomenon of conversion polymorphism in Bi-containing metastable perovskites. *Chem. Commun.* **2019**, *55*, 4683–4686. [CrossRef] [PubMed]
42. Fedorchenko, A.; Fertman, E.L.; Salak, A.N.; Desnenko, V.A.; Čižmár, E.; Feher, A.; Vaisburd, A.I.; Olekhnovich, N.M.; Pushkarev, A.V.; Radyush, Y.V.; et al. Unusual magnetic properties of the polar orthorhombic $BiFe_{0.5}Sc_{0.5}O_3$ perovskite. *J. Magn. Magn. Mater.* **2018**, *465*, 328–332. [CrossRef]
43. Fertman, E.L.; Fedorchenko, A.V.; Desnenko, V.A.; Shvartsman, V.V.; Lupascu, D.C.; Salamon, S.; Wende, H.; Vaisburd, A.I.; Stanulis, A.; Ramanauskas, R.; et al. Exchange bias effect in bulk multiferroic $BiFe_{0.5}Sc_{0.5}O_3$. *AIP Adv.* **2020**, *10*, 045102. [CrossRef]
44. Fertman, E.L.; Fedorchenko, A.V.; Čižmár, E.; Vorobiov, S.; Feher, A.; Radyush, Y.V.; Pushkarev, A.V.; Olekhnovich, N.M.; Stanulis, A.; Barron, A.R.; et al. Magnetic diagram of the high-pressure stabilized multiferroic perovskites of the $BiFe_{1-y}Sc_yO_3$ series. *Crystals* **2020**, *10*, 950. [CrossRef]
45. Shvartsman, V.V.; Khalyavin, D.D.; Olekhnovich, N.M.; Pushkarev, A.V.; Radyush, Y.V.; Salak, A.N. Spontaneous and induced ferroelectricity in the $BiFe_{1-x}Sc_xO_3$ perovskite ceramics. *Phys. Status Solidi A* **2021**, *218*, 2100173. [CrossRef]
46. Prosandeev, S.A.; Khalyavin, D.D.; Raevski, I.P.; Salak, A.N.; Olekhnovich, N.M.; Pushkarev, A.V.; Radyush, Y.V. Complex antipolar $\sqrt{2} \times 4 \times 2\sqrt{2}$ structure with *Pnma* symmetry in $BiFeO_3$ and $BiFe_{1/2}Sc_{1/2}O_3$: First-principles calculations. *Phys. Rev. B* **2014**, *90*, 054110. [CrossRef]
47. Belik, A.A.; Rusakov, D.A.; Furubayashi, T.; Takayama-Muromachi, E. $BiGaO_3$-based perovskites: A large family of polar materials. *Chem. Mater.* **2012**, *24*, 3056–3064. [CrossRef]
48. Belik, A.A.; Abakumov, A.M.; Tsirlin, A.A.; Hadermann, J.; Kim, J.; Van Tandeloo, G.; Takayama-Muromachi, E. Structure and magnetic properties of $BiFe_{0.75}Mn_{0.25}O_3$ perovskite prepared at ambient and high pressure. *Chem. Mater.* **2011**, *42*, 4505–4514. [CrossRef]
49. Belik, A.A. Two perovskite modifications of $BiFe_{0.6}Mn_{0.4}O_3$ prepared by high pressure and post-synthesis annealing at ambient pressure. *Inorganics* **2024**, *12*, 226. [CrossRef]
50. Belik, A.A. Magnetic properties of solid solutions between $BiCrO_3$ and $BiGaO_3$ with perovskite structures. *Sci. Technol. Adv. Mater.* **2015**, *16*, 026003. [CrossRef]
51. Belik, A.A. Solid solutions between $BiMnO_3$ and $BiCrO_3$. *Inorg. Chem.* **2016**, *55*, 12348–12356. [CrossRef] [PubMed]

52. Baettig, P.; Spaldin, N.A. Ab initio prediction of a multiferroic with large polarization and magnetization. *Appl. Phys. Lett.* **2005**, *86*, 012505. [CrossRef]
53. Suchomel, M.R.; Thomas, C.I.; Allix, M.; Rosseinsky, M.J.; Fogg, A.M.; Thomas, M.F. High pressure bulk synthesis and characterization of the predicted multiferroic $Bi(Fe_{1/2}Cr_{1/2})O_3$. *Appl. Phys. Lett.* **2007**, *90*, 112909. [CrossRef]
54. Palaimiene, E.; Gribauskaite, V.; Banys, J.; Pushkarev, A.V.; Radyush, Y.V.; Olekhnovich, N.M.; Cardoso, J.P.V.; Salak, A.N. Dielectric characterization of the $BiFe_{0.5}Cr_{0.5}O_3$ ceramics. *Lith. J. Phys.* **2022**, *62*, 206–211. [CrossRef]
55. Goffinet, M.; Iniguez, J.; Ghosez, P. First-principles study of a pressure-induced spin transition in multiferroic Bi_2FeCrO_6. *Phys. Rev. B* **2012**, *86*, 024415. [CrossRef]
56. Himcinschi, C.; Drechsler, F.; Walch, D.S.; Bhatnagar, A.; Belik, A.A.; Kortus, J. Unexpected Phonon Behaviour in $BiFe_xCr_{1-x}O_3$, a Material System Different from Its $BiFeO_3$ and $BiCrO_3$ Parents. *Nanomaterials* **2022**, *12*, 1607. [CrossRef]
57. Kan, Y.; Liu, J.; Chen, R.; Liu, Y.; Wang, H.; Long, M.; Tian, B.; Chu, J.; Chen, Y.; Sun, L. Enhanced ferroelectric photovoltaic performance of Bi_2FeCrO_6 thin films for neuromorphic computing applications. *Appl. Phys. Lett.* **2024**, *124*, 112906. [CrossRef]
58. Henning, X.; Schlur, L.; Wendling, L.; Fix, T.; Colis, S.; Dinia, A.; Alexe, M.; Rastei, M.V. Interfacial photovoltaic effects in ferroelectric Bi_2FeCrO_6 thin films. *Phys. Rev. Mater.* **2025**, *9*, 024403. [CrossRef]
59. Chang, F.; Zhang, N.; Yang, F.; Wang, S.; Song, G. Effect of Cr substitution on the structure and electrical properties of $BiFeO_3$ ceramics. *J. Phys. D Appl. Phys.* **2007**, *40*, 7799–7803. [CrossRef]
60. Luo, B.-C.; Chen, C.-L.; Jin, K.-X. Low temperature properties of multiferroic $BiFe_{0.9}Cr_{0.1}O_3$ compound. *Solid State Commun.* **2011**, *151*, 712–715. [CrossRef]
61. Rusakov, V.S.; Pokatilov, V.S.; Sigov, A.S.; Belik, A.A.; Matsnev, M.E. Changes in the magnetic structure of multiferroic $BiFe_{0.80}Cr_{0.20}O_3$ with temperature. *Phys. Solid State* **2019**, *61*, 1030–1036. [CrossRef]
62. Raevski, I.P.; Kubrin, S.P.; Pushkarev, A.V.; Olekhnovich, N.M.; Radyush, Y.V.; Titov, V.V.; Malitskaya, M.A.; Raevskaya, S.I.; Chen, H. The effect of Cr substitution for Fe on the structure and magnetic properties of $BiFeO_3$ multiferroic. *Ferroelectrics* **2018**, *525*, 1–10. [CrossRef]
63. Kubrin, S.P.; Raevski, I.P.; Olekhnovich, N.M.; Pushkarev, A.V.; Radyush, Y.V.; Titov, V.V.; Malitskaya, M.A.; Li, G.R.; Raevskaya, S.I. Mössbauer study of the effect of cation substitutions on the magnetic phase transitions in $BiFe_{1-x}Cr_xO_3$ and (1–x)$BiFeO_3$–x$PbFe_{0.5}Sb_{0.5}O_3$ solid solutions. *Crystal. Rep.* **2020**, *65*, 338–342. [CrossRef]
64. Arafat, S.S. Structural transition and magnetic properties of high Cr-doped $BiFeO_3$ ceramic. *Cerâmica* **2020**, *66*, 114–118. [CrossRef]
65. Corker, D.L.; Glazer, A.M.; Dec, J.; Roleder, K.; Whatmore, R.W. A re-investigation of the crystal structure of the perovskite $PbZrO_3$ by X-ray and neutron diffraction. *Acta Crystallogr. Sect. B Struct. Sci.* **1997**, *53*, 135–142. [CrossRef]
66. Teslic, S.; Egami, T. Atomic structure of $PbZrO_3$ determined by pulsed neutron diffraction. *Acta Crystallogr. Sect. B Struct. Sci.* **1998**, *54*, 750–765. [CrossRef]
67. Shannon, R. Revised effective ionic radii and systematic studies of interatomic distances in halides and chalcogenides. *Acta Crystallogr. Sect. A* **1976**, *32*, 751–767. [CrossRef]
68. Rusakov, D.A.; Abakumov, A.M.; Yamaura, K.; Belik, A.A.; Van Tendeloo, G.; Takayama-Muromachi, E. Structural evolution of the $BiFeO_3-LaFeO_3$ system. *Chem. Mater.* **2011**, *23*, 285–292. [CrossRef]
69. Troyanchuk, I.O.; Karpinsky, D.V.; Bushinsky, M.V.; Khomchenko, V.A.; Kakazei, G.N.; Araujo, J.P.; Tovar, M.; Sikolenko, V.; Efimov, V.; Kholkin, A.L. Isothermal structural transitions, magnetization and large piezoelectric response in $Bi_{1-x}La_xFeO_3$ perovskites. *Phys. Rev. B* **2011**, *83*, 054109. [CrossRef]
70. Cheng, C.-J.; Kan, D.; Lim, S.-H.; McKenzie, W.R.; Munroe, P.R.; Salamanca-Riba, L.G.; Withers, R.L.; Takeuchi, I.; Nagarajan, V. Structural transitions and complex domain structures across a ferroelectric-to-antiferroelectric phase boundary in epitaxial Sm-doped $BiFeO_3$ thin films. *Phys. Rev. B* **2009**, *80*, 014109. [CrossRef]
71. Kalantari, K.; Sterianou, I.; Karimi, S.; Ferrarelli, M.C.; Miao, S.; Sinclair, D.C.; Reaney, I.M. Ti-doping to reduce conductivity in $Bi_{0.85}Nd_{0.15}FeO_3$ ceramics. *Adv. Funct. Mater.* **2011**, *21*, 3737–3743. [CrossRef]
72. Carvalho, T.T.; Fernandes, J.R.A.; Perez de la Cruz, J.; Vidal, J.V.; Sobolev, N.A.; Figueiras, F.; Das, S.; Amaral, V.S.; Almeida, A.; Agostinho Moreira, J.; et al. Room temperature structure and multiferroic properties in $Bi_{0.7}La_{0.3}FeO_3$ ceramics. *J. Alloys Compd.* **2013**, *554*, 97–103. [CrossRef]
73. Gomes, M.M.; Carvalho, T.T.; Manjunath, B.; Vilarinho, R.; Gibbs, A.S.; Knight, K.S.; Paixao, J.A.; Amaral, V.S.; Almeida, A.; Tavares, P.B.; et al. Disentangling the phase sequence and correlated critical properties in $Bi_{0.7}La_{0.3}FeO_3$ by structural studies. *Phys. Rev. B* **2021**, *104*, 174109. [CrossRef]
74. Kumar, A.; Yusuf, S.M. The phenomenon of negative magnetization and its implications. *Phys. Rep.* **2015**, *556*, 1–34. [CrossRef]
75. Billoni, O.V.; Pomiro, F.; Cannas, S.A.; Martin, C.; Maignan, A.; Carbonio, R.E. Magnetization reversal in mixed ferrite-chromite perovskites with non magnetic cation on the A-site. *J. Phys. Condens. Matter* **2016**, *28*, 476003. [CrossRef]
76. Dasari, N.; Mandal, P.; Sundaresan, A.; Vidhyadhiraja, N.S. Weak ferromagnetism and magnetization reversal in $YFe_{1-x}Cr_xO_3$. *Europhys. Lett.* **2012**, *99*, 17008. [CrossRef]

77. Kawaguchi, S.; Takemoto, M.; Osaka, K.; Nishibori, E.; Moriyoshi, C.; Kubota, Y.; Kuroiwa, Y.; Sugimoto, K. High-throughput powder diffraction measurement system consisting of multiple MYTHEN detectors at beamline BL02B2 of SPring-8. *Rev. Sci. Instrum.* **2017**, *88*, 085111. [CrossRef]
78. Kawaguchi, S.; Takemoto, M.; Tanaka, H.; Hiraide, S.; Sugimoto, K.; Kubota, Y. Fast continuous measurement of synchrotron powder diffraction synchronized with controlling gas and vapour pressures at beamline BL02B2 of SPring-8. *J. Synchrotron Rad.* **2020**, *27*, 616–624. [CrossRef]
79. Izumi, F.; Ikeda, T. A Rietveld-analysis program RIETAN-98 and its applications to zeolites. *Mater. Sci. Forum* **2000**, *321–324*, 198–205. [CrossRef]